Measurement of D/H and 13C/12C ratios in methane ice on Eris and Makemake: Evidence for internal activity

W.M. Grundy, I. Wong, C.R. Glein, S. Protopapa, B.J. Holler, J.C. Cook, J.A. Stansberry, J.I. Lunine, A.H. Parker, H.B. Hammel, et al.

Measurement of D/H and $^{13}C/^{12}C$ Ratios in Methane Ice on Eris and Makemake: Evidence for Internal Activity

W.M. Grundy[1,2], I. Wong[3,4], C.R. Glein[5], S. Protopapa[5], B.J. Holler[6], J.C. Cook[7], J.A. Stansberry[6], J.I. Lunine[8], A.H. Parker[9], H.B. Hammel[10], S.N. Milam[3], R. Brunetto[11], N. Pinilla-Alonso[12], A.C. de Souza Feliciano[12], J.P. Emery[2], and J. Licandro[13]

1. Lowell Observatory, Flagstaff Arizona.
2. Northern Arizona University, Flagstaff Arizona.
3. NASA Goddard Space Flight Center, Greenbelt Maryland.
4. American University, Washington DC.
5. Southwest Research Institute, San Antonio Texas.
6. Space Telescope Science Institute, Baltimore Maryland.
7. Pinhead Institute, Telluride Colorado.
8. Cornell University, Ithaca New York.
9. SETI Institute, Mountain View California.
10. Association of Universities for Research in Astronomy, Washington DC.
11. Université Paris-Saclay, CNRS, Paris, France.
12. Florida Space Institute, University of Central Florida, Orlando Florida.
13. Instituto de Astrofísica de Canarias (IAC), La Laguna, Spain.

— Revised for *Icarus* —

Primary contact: Will Grundy
Mailing address: Lowell Observatory, 1400 W. Mars Hill Rd., Flagstaff AZ 86001
E-mail: W.Grundy@lowell.edu
Voice: 928-233-3231

Running head: Eris and Makemake D/H and $^{13}C/^{12}C$
Manuscript pages: 35
Figures: 5
Tables: 0

Keywords: *Dwarf planets*; *Ices; Transneptunian objects*; *Infrared observations*; *Cosmochemistry*.

Abstract

James Webb Space Telescope's NIRSpec infrared imaging spectrometer observed the outer solar system dwarf planets Eris and Makemake in reflected sunlight at wavelengths spanning 1 through 5 microns. Both objects have high albedo surfaces that are rich in methane ice, with a texture that permits long optical path lengths through the ice for solar photons. There is evidence for N_2 ice absorption around 4.2 µm on Eris, though not on Makemake. No CO ice absorption is seen at 4.67 µm on either body. For the first time, absorption bands of two heavy isotopologues of methane are observed at 2.615 µm ($^{13}CH_4$), 4.33 µm ($^{12}CH_3D$), and 4.57 µm ($^{12}CH_3D$). These bands enable us to measure D/H ratios of $(2.5 \pm 0.5) \times 10^{-4}$ and $(2.9 \pm 0.6) \times 10^{-4}$, along with $^{13}C/^{12}C$ ratios of 0.012 ± 0.002 and 0.010 ± 0.003 in the surface methane ices of Eris and Makemake, respectively. The measured D/H ratios are much lower than that of presumably primordial methane in comet 67P/Churyumov-Gerasimenko, but they are similar to D/H ratios in water in many comets and larger outer solar system objects. This similarity suggests that the hydrogen atoms in methane on Eris and Makemake originated from water, indicative of geochemical processes in past or even ongoing hot environments in their deep interiors. The $^{13}C/^{12}C$ ratios are consistent with commonly observed solar system values, suggesting no substantial enrichment in ^{13}C as could happen if the methane currently on their surfaces was the residue of a much larger inventory that had mostly been lost to space. Possible explanations include geologically recent outgassing from the interiors as well as processes that cycle the surface methane inventory to keep the uppermost surfaces refreshed.

Introduction

The outer solar system is endowed with a large and diverse population of small icy planets that provide rich opportunities for comparative planetology. Those that are massive and cold enough to retain volatile ices such as nitrogen and methane are an especially interesting clan (Schaller & Brown 2007; Johnson et al. 2015). Changing seasonal patterns of insolation drive sublimation and bulk transport of gravitationally bound volatile ices (Trafton et al. 1998). The seasonal redistribution of these ices segregates them from darker materials (e.g. radiolytic compounds, meteoritic dust). This keeps their albedo high and temperature low. The phase changes between solid and vapor enable thermal energy, primarily from sunlight, to produce mechanical effects, sculpting their surfaces and creating diverse landforms (e.g., Moore et al.

2017; Stern et al. 2018; Grundy 2019). Deep inside bodies that contain substantial inventories of rock, heat from decay of radionuclides may power the production of volatiles (McKinnon et al. 2021). Objects that still possess abundant methane at present include Triton, Pluto, Eris, and Makemake, in order of increasing methane absorption band depths observed in ground-based spectra (e.g. Cruikshank et al. 1993; Owen et al. 1993; Licandro et al. 2006a,b; Brown et al. 2005, 2007; Dumas et al. 2007; Tegler et al. 2007, 2008, 2010, 2012; Alvarez-Candal et al. 2011).

Eris and Makemake, the bodies with the strongest methane absorption bands, can provide us with novel comparisons with other transneptunian dwarf planets. Eris is intermediate in mass between Triton and Pluto (Brown & Schaller 2007) but slightly smaller (diameter 2326 km; Sicardy et al. 2011) than Pluto (2377 km; Nimmo et al. 2017) and with a higher bulk density than both (Sicardy et al. 2011; Holler et al. 2021). The higher density implies a rock-rich composition, providing abundant internal heat from decay of long-lived radionuclides. Eris orbits much further from the Sun than Pluto, at a mean distance of 68 AU, but its high eccentricity brings it to 38 AU at perihelion and 98 AU at aphelion, resulting in nearly a factor of 7 difference in incident sunlight over the course of its orbit. Photometric observations show that Eris has a very high albedo (Mueller et al. 2019) and exhibits very little photometric variability as it spins on its axis (e.g., Carraro et al. 2006; Maris & Carraro 2008). The low lightcurve amplitude makes the length of Eris' day difficult to determine. A variety of tentative rotational periods have been reported (e.g., Duffard et al. 2008; Roe et al. 2008) but a combination of ground- and space-based observations has recently revealed it to be synchronous with its satellite Dysnomia's ~15.8 day orbital period (Bernstein et al. 2023; Szakáts et al. 2023; Nimmo & Brown 2023), longer than the ~6 day diurnal cycles of Pluto and Triton. If it is assumed that Eris' spin axis is aligned with Dysnomia's orbit pole, this would imply a high obliquity of 78°, with important implications for Eris' seasons (e.g., Holler et al. 2021).

Makemake is a somewhat smaller body with equatorial and polar axes in the range between 1400 and 1500 km (Ortiz et al. 2012; Brown 2013), intermediate in size between Pluto and Charon. Makemake is similar to Eris in having its perihelion at 38 AU, though its aphelion is much closer than that of Eris, at only 53 AU, owing to its smaller semimajor axis and eccentricity. Makemake is also like Eris in having a very high albedo and low lightcurve variability. Various rotation periods have been reported, ranging from 8 to 23 hours (e.g., Ortiz

et al. 2007; Heinze & deLahunta 2009; Hromakina et al. 2019). The discovery of a satellite (Parker et al. 2016) opens the prospect of determining an accurate mass and density for Makemake. Makemake, Eris, and Pluto all share similar linear polarization at low phase angles (Belskaya et al. 2012), presumably related to the light scattering properties of their seasonally mobile methane ice.

The high abundance of methane raises important questions about Eris and Makemake. First, what is the methane's source? Because comets generally contain methane, we might assume that methane was accreted from the solar nebula into pebbles and thence planetesimals at large heliocentric distances (e.g., Schaller & Brown 2007), but it is also possible that methane might have been produced in the interiors of Eris and Makemake, by analogy with geochemical processes that have been proposed for Pluto (McKinnon et al. 2021) and Titan (Glein 2015). Second, how do they maintain their high albedos? Methane ice exposed to energetic space radiation is rapidly processed into heavier hydrocarbons and ultimately dark, reddish tholin-like macro-molecules (e.g., Thompson et al. 1987; Stern et al. 1988; Brunetto et al. 2006). Inspired by the diverse landforms of Pluto and Triton, a variety of resurfacing scenarios can be imagined. Seasonal sublimation and condensation cycles could distill methane from its darker, more refractory radiation products, enabling the volatile methane to remain on top (Hofgartner et al. 2019). This mechanism could make them "bladed planets" by analogy to Pluto's methane-rich bladed terrain, which features high albedos and relatively neutral colors consistent with low abundances of dark, reddish radiolytic products (e.g., Moore et al. 2017; Hofgartner et al. 2023). If the surface methane deposit is thick enough, convective glacial overturn could continually refresh its surface, making Eris and Makemake more like "Sputnik planets" (Grundy & Umurhan 2017) reminiscent of Pluto's Sputnik Planitia (e.g., McKinnon et al. 2016), another region noteworthy for its high albedo and relatively neutral colors (e.g., Grundy et al. 2018; Protopapa et al. 2020; Olkin et al. 2021).

Other volatile ices provide additional pieces to the puzzle of dwarf planet origin and evolution. Either the presence or apparent absence of certain species can be illuminating. For example, we might ask how much N_2 and CO ices are present, and what is their influence on resurfacing processes? Where might they have come from? The presence of N_2 had been inferred indirectly from its influence on the CH_4 bands seen on Eris and Makemake (e.g., Licandro et al. 2006a,b; Merlin et al. 2009; Tegler et al. 2008, 2010; Lorenzi et al. 2015), but it

had not previously been directly detected. CO has not been detected on either body, though it is seen on Triton and Pluto and is abundant in comets. Heavier hydrocarbons can be produced via radiolysis or photolysis of methane (Bennett et al. 2006). C_2H_4 and C_2H_6 have been reported on Makemake (Brown et al. 2007, 2015) though not on Eris. Materials like H_2O, CO_2, and CH_3OH might also be expected, since they have been detected on numerous other outer solar system objects. Although these species are volatile in warmer environments, they would be inert at the surface temperatures of Eris and Makemake, so their presence could potentially be indicative of a process that works against their burial under more mobile materials or produces them at the surface such as via exogenic delivery or radiolytic production.

Observations and data reduction

James Webb Space Telescope (JWST) observed Eris on 2022 August 30 as part of Cycle 1 Guaranteed Time Observations (GTO) Program 1191. At that time Eris was 95.1 AU from JWST and 95.8 AU from the Sun with a solar phase angle of 0.5°. The observations used the integral field unit (IFU) of the Near-Infrared Spectrograph (NIRSpec) instrument. The IFU has a field of view of 3”x3” and a spatial pixel scale of 0.1”. Pairs of dithered exposures were obtained with three medium-resolution grating-filter combinations in sequence – G140M/F100LP, G235M/F170LP, and G395M/F290LP – to provide continuous wavelength coverage from 0.98 to 5.25 μm at a resolving power ($\lambda/\Delta\lambda$) of about 1000. The total exposure times in the three spectral settings were 613, 613, and 1196 seconds, respectively, yielding a combined exposure time of 2422 seconds. To optimize the detector noise performance, the NRSIRS2RAPID readout method was selected, which intersperses reference pixel reads with science pixel readouts (Moseley et al. 2010; Rauscher et al. 2012).

Makemake was observed on 2023 January 29 as part of Cycle 1 GTO Program 1254, when the target had observer-centric and heliocentric ranges of 52.2 and 52.7 AU, respectively, and a solar phase angle of 1.0°. The same gratings, dither pattern, and readout method were used for this observation, with per-grating exposure times of 521, 934, and 1780 seconds and a combined exposure time of 3035 seconds.

Data reduction and spectral extraction were carried out using a dedicated pipeline developed for NIRSpec IFU spectral observations. The core data processing functions were handled by Version 1.11.3 of the official JWST pipeline (Bushouse et al. 2022), with relevant calibration

reference files supplied from context *jwst_1100.pmap* of the JWST Calibration Reference Data System (CRDS). The raw uncalibrated images (*uncal.fits* files) were first passed through Stage 1 of the JWST pipeline (*calwebb_detector1*), which converts the ramps of non-destructive detector readouts into 2D count rate images (*rate.fits* files) that are corrected for the bias level, dark current, non-linearity, and cosmic ray effects. While the IRS^2 readout greatly reduces read noise, there are residual systematic offsets in noise level across the detector, which manifest as column striping in the count rate images. To address this, a column-by-column read noise correction was applied by masking on-sky pixels to isolate the non-illuminated region, calculating the 200-pixel-wide moving median along each column, and subtracting the median array from the column pixel values. The noise-corrected *rate.fits* files were then processed through Stage 2 of the JWST pipeline (*calwebb_spec2*) to arrive at a set of 6 flat-fielded, distortion-corrected, wavelength-calibrated, and flux-calibrated IFU data cubes (*s3d.fits* files) – one for each dither position and grating. An IFU cube contains a stack of spatially rectified 2D image slices, each one corresponding to a single wavelength in the uniformly spaced wavelength solution. Figure 1 shows examples of the IFU cubes, collapsed along the wavelength axis, for both Eris and Makemake. The JWST pipeline outputs the IFU data cubes with units of MJy sr^{-1}. Prior to spectral extraction, the cubes were multiplied by the corresponding spatial pixel area contained in the headers to convert to irradiance units (MJy pixel^{-1}).

Our data processing pipeline utilizes a specialized empirical point-spread function (PSF) fitting technique to extract the target's irradiance spectrum. The global source centroid was computed by collapsing the IFU cube along the wavelength axis and using a 2D Gaussian fit to estimate the peak position, rounded to the nearest integer pixel. To construct the template PSF at a given wavelength k, a median image slice was constructed by averaging image slices in the range $[k-W, k+W]$, where W is an adjustable window width. The background region was defined to be all pixels outside of a square box of side length L_b centered on the centroid. All pixels with a nonzero data quality value were masked, and the median flux within the background region was subtracted from the median image. The template PSF of the target was defined within a box of side length L_a centered on the centroid and was set equal to the flux of the median image slice, normalized to unit sum. The same values of W, L_a, and L_b were used for all wavelengths. All pixels within the outer background region were fixed to zero, while pixels between the regions defined by L_a and L_b were masked and not considered in the subsequent extraction. The source

flux was then computed via a least-squares fit of the template PSF to the image slice k using Levenberg-Marquardt χ^2 minimization. The flux model consisted of the template PSF, multiplied by a scaling factor, along with an additive background level. Both the scaling factor and background level were free parameters in the fit, and the χ^2 was weighted by the pixel flux uncertainties calculated by the JWST pipeline. The least-squares fitting was done iteratively, each time masking 5-σ outlier pixels until none remained. This PSF fitting procedure was carried out on every image slice, with the background-subtracted irradiance of the target at each wavelength provided by the best-fit scaling factor.

Our empirical PSF fitting technique is ideal for small body spectral extraction (i.e., point sources), because it provides greatly increased signal-to-noise over standard circular or square aperture extraction methods, while self-consistently accounting for wavelength-dependent changes in both source position and PSF shape and being more robust to bad pixels within the fitting region. We experimented with various values for W, L_a, and L_b. For NIRSpec IFU data cubes, there are wavelength-dependent oscillations in the source PSF width due to numerical artifacts that arise from the flux resampling during the cube building process. These oscillations can occur at scales as small as 30-40 image slices, so in order to accurately model the local PSF shape, we must use narrower window widths. We chose $W = 10$ when producing the spectra presented in this paper; varying the window widths between 5 and 15 produced no discernible systematic changes to the resultant flux values and overall scatter in the spectra.

When constructing template PSFs and extracting fluxes, we found that establishing a sizeable buffer region between the inner flux extraction region and the outer background region (i.e., $L_a < L_b$) yielded better signal-to-noise and reduced spectral scatter. As shown in Fig. 1, NIRSpec point-source PSFs have a large spatial extent. However, the outer regions of the diffraction pattern have relatively low signal-to-noise and are only several standard deviations above the overall background level. It follows that low-level detector artifacts and unflagged bad pixels can noticeably bias the template PSF scale factor in this region, which otherwise does not contribute appreciably to the total source flux. Moreover, in the case of Eris, the small satellite Dysnomia lies approximately 4 pixels from the primary centroid and can be discerned in the wavelength-collapsed IFU image slice (see Fig. 1). We therefore selected relatively compact flux extraction boxes. For Eris, $L_a = 5$ px was chosen for all dither positions and grating settings in order to avoid the peak of the secondary's PSF, while for Makemake, where the satellite is not

222 discernible or expected to contribute significantly to the flux, we used L_a = 9 px. Varying L_a by
223 several pixels in either direction did not substantively affect the final spectra, even in the case of
224 Eris, indicating that the contamination from Dysnomia's flux is negligible. In all cases, we set
225 L_b = 21 px for the inner edge of the background region, which comfortably excludes all of the
226 target PSF. The regions on the image slices corresponding to these spectral extraction parameter
227 choices are indicated in Fig. 1. After extracting the irradiance spectrum for each dither position,
228 we applied a 20 point wide moving-median filter to remove remaining 5-σ outliers and combined
229 the two dither spectra together using a simple mean.

230 A small but non-negligible fraction of the total source PSF falls outside of the PSF fitting
231 region denoted by L_a. We used NIRSpec flux calibration observations of the G2V-type standard
232 star P330E obtained with the same grating settings (Cycle 1 Calibration Program 1538; PI: K.
233 Gordon) to derive wavelength-dependent aperture correction curves and recover the full source
234 irradiance of Eris and Makemake. After the uncalibrated data files from the standard star
235 observation were reduced using an identical process to the Eris and Makemake data reductions,
236 we extracted the star's flux using PSF fitting within boxes of sizes L_a = 5 and 9 px. The resultant
237 stellar spectra were then divided by the CALSPEC reference spectrum of P330E convolved to
238 the sampling of the NIRSpec data (Bohlin et al. 2014) to compute the ratio array that quantifies
239 the fraction of the total calibrated source flux within the corresponding extraction regions. By
240 fitting cubic functions to these ratio arrays, we obtained empirical correction curves for each flux
241 extraction region size and grating setting and divided them from the previously extracted spectra
242 of Eris and Makemake to generate the corrected absolute flux spectra. We divided the irradiance
243 of each object by the G-star spectrum that was extracted using the same L_a value to get
244 reflectance spectra. This process self-consistently accounts for both the flux losses outside of the
245 extraction region and any minor wavelength-dependent instrumental systematics that are shared
246 by all NIRSpec IFU spectra. A handful of visible outliers in the spectra remained at this stage,
247 mostly attributable to poorly divided stellar lines, and we manually trimmed these. We scaled
248 the reflectance to $I/F = \pi I r^2 / F_\odot$, where I is the radiance at the detector defined as power per unit
249 area per unit solid angle, r is the target heliocentric distance in AU, and $F_\odot$ is the solar flux at 1
250 AU. The latter was computed using the Planetary Spectrum Generator (Villanueva et al. 2018,
251 2022) and was scaled in a continuum region to the CALSPEC solar spectrum to recover units of
252 MJy. I was computed by dividing the target flux corrected for light losses by the target area in

pixel units and the pixel solid angle. The radii used to determine the target area of Eris and Makemake are 1163 and 715 km, respectively.

Spectral interpretation and modeling

The complete JWST-NIRSpec reflectance spectrum of Eris is shown in Fig. 2. Previous visible and near-infrared reflectance spectra of Eris indicated a surface dominated by methane ice (e.g., Brown et al. 2005; Licandro et al. 2006b; Dumas et al. 2007; Abernathy et al. 2009; Merlin et al. 2009; Alvarez-Candal et al. 2011). These papers observed numerous methane vibrational combination and overtone bands between 1 and 2.5 μm that also appear in the JWST spectrum. JWST's extension of spectral coverage out beyond 5 μm reveals four strong infrared CH_4 ice bands that had not previously been detected at Eris. These bands, at 2.60, 3.32, 3.55, and 3.85 μm, correspond to the $3\nu_4$, ν_3, $\nu_2 + \nu_4$, and $2\nu_4$ vibrational modes in methane ice (e.g., Ewing 1964; Calvani et al. 1989, 1992; Grundy et al. 2002). CH_3D bands at 4.33 and 4.56 μm are also evident, corresponding to $2\nu_6$ and ν_2 vibrational modes, respectively (Grundy et al. 2011). Much weaker CH_3D bands at 2.47 ($2\nu_3 + \nu_5$) and 2.87 μm ($3\nu_6$ and $\nu_2 + \nu_3$) are marginally seen, too. Observation of these CH_3D bands provides an opportunity to measure the D/H ratio in Eris' methane ice. Apart from $^{12}CH_4$, CH_3D, $^{13}CH_4$, and N_2 (see below), we have not unambiguously identified any other species in the new Eris spectrum. These non-detections include hydrocarbons like ethane, ethylene, and acetylene that are readily produced through radiolysis and photolysis of methane (e.g., Bennett et al. 2006), as well as H_2O, CO_2, CH_3OH, HCN, and NH_3 that have been detected on the surfaces of a number of other outer solar system bodies.

Quantitative information about solid planetary surfaces can be extracted from reflectance spectra by using a radiative transfer model to account for the wavelength dependent scattering of light by small particles in the planetary surface. We use the Hapke model for this purpose (e.g., Hapke 2012 and references therein). This model accounts for the wavelength-dependent optical behavior of individual regolith particles via two parameters: the single-scattering albedo (w) that expresses the fraction of light that is not absorbed in an interaction between a ray of light and a particle, and the single-scattering phase function ($P_{(g)}$) that describes the angular distribution of light scattering by the particle. We employ three commonly used simplifications to the model. First, we set the opposition effect and macroscopic roughness to fixed values, since these can generally only be constrained with multi-angular observations. Following Verbiscer et al. (2022)

we set the opposition width parameter h to 0.057, the amplitude parameter B_0 to 0.36, and the macroscopic roughness θ to 20°. Second, we assume that only w is a function of wavelength. Third, since we only need to evaluate $P_{(g)}$ at the single phase angle g of the JWST observations, we treat $P_{(g)}$ as a constant rather than as a function of g, which is feasible in the IMSA (isotropic multiple-scattering approximation) variant of Hapke's model. To obtain w for a particle of a specific material, we use the equivalent slab model described by Hapke (2012). Given a particle size and optical constants (n and k) for a given wavelength, this model provides w at that wavelength. An intimate mixture of different sorts of particles can be simulated by averaging their w values, weighted by the particles' fractional contributions to the surface area.

Crucial model inputs are the optical constants of candidate materials at relevant wavelengths and temperatures. For methane ice we used the higher dynamic range absorption data from Grundy et al. (2002) along with the refractive index data from Gerakines & Hudson (2020). To treat the D/H ratio in the methane ice as a free parameter we used the data and methodology of Grundy et al. (2011). This works by first removing the CH_3D contribution present in the published methane ice optical constants, and then adding back in the appropriate amount of CH_3D absorption corresponding to a specific D/H ratio, accounting for the fact that a methane molecule has four hydrogen atoms. Other optical constants used in this work include nitrogen ice, taken from a spectrum used in the analysis of Grundy et al. (2011) and carbon monoxide ice from Ehrenfreund et al. (1996).

The parameters of the model were iteratively modified to match the observed spectrum using the downhill simplex ("amoeba"; Nelder & Mead 1965) algorithm to minimize χ^2 between model and observation, re-computing synthetic optical constants for methane with the model D/H ratio as needed within the iterative chi-squared minimization loop. We fitted the model to wavelengths from 1.4 to 4.8 µm, with wavelengths between 4.4 and 4.7 µm given triple weight to force the model to be especially attentive where the ν_2 CH_3D band (4.56 µm) is relatively free of interference from other absorbers, making it the most diagnostic band for the D/H ratio. This region of increased weighting also limits dependence on the 4.25 µm region where some of the laboratory optical constants data show contamination from CO_2 vapor. Where many bands of the same species are observed in a single spectrum, the particle size implied by the weaker bands tends to be larger than that implied by the stronger bands, indicating a more complex surface configuration than just a single particle size across the entire planet. Modelers employ a variety

of strategies to handle this complexity, adding distinct terrain types, stratigraphic layers, or particle types. We used two different particle sizes for this purpose, which allowed the model to closely reproduce the data. The parameters that were adjusted were the D/H ratio in methane via the methane optical constants, the particle sizes and relative abundance of two sizes of methane ice particles both sharing the same optical constants, a scalar value for $P_{(g)}$, and nitrogen and carbon monoxide ice abundances. N_2 and CO were treated as minority contaminants dissolved in the methane ice by means of a volume-weighted linear mixture of the optical constants of pure methane plus the two contaminants.

The best fit Eris model is shown in Fig. 2. The derived parameters are D/H ratio 2.5×10^{-4}, methane grain sizes 0.39 and 0.02 cm diameter (with the smaller particles representing 3.2% of the total, by volume). Eris' high albedo requires a moderately high value for $P_{(g)}$ of 1.4. This could indicate a back-scattering single-scattering phase function, though it could also be a back-scattering lobe that is coupled with a forward-scattering lobe that we are not sensitive to owing to the small phase angle of the observation. Alternatively, the opposition effect could be stronger at these wavelengths in which case B_0 should be closer to unity. Any errors in the I/F calibration would mostly be accommodated by shifts in the $P_{(g)}$ value. The model includes 22% N_2 ice by volume to account for a broad absorption between 4.0 and 4.3 µm, as shown in the left panel of Fig. 3. This absorption is weak, since N_2 is a homonuclear molecule without an intrinsic dipole moment. Interaction with neighboring molecules can induce a transient dipole, so this type of absorption band has been referred to as collisionally induced absorption (e.g., Van Kranendonk 1957; Shapiro & Gush 1966). There is no evidence for absorption by the vibrational fundamental band of CO ice at 4.67 µm. We should note that the available optical constants for CO and N_2 are not for those materials dissolved in CH_4 ice, but rather for the pure species. Studies of CO dissolved in N_2 ice do show modest differences in band shapes relative to pure CO ice (Quirico & Schmitt 1997a), so laboratory studies to investigate the spectral behaviors of both ices when diluted in CH_4 ice are called for.

A portion of the Makemake spectrum was made available to us ahead of publication for the purpose of isotopic analysis (S. Protopapa personal communication). Like Eris, the Makemake spectrum is methane-dominated and CH_3D bands are clearly evident. We applied the same model to it, except with $B_0 = 1$, $h = 0.11$, and $\theta = 5°$ (Verbiscer et al. 2022), and fitting to wavelengths between 3.4 and 4.8 µm (fitting to the Eris data in just this smaller range resulted in

345 little change in D/H). The data and model are shown in the right panel of Fig. 3. Other materials
346 not included in our model are clearly present in the Makemake spectrum, to be discussed in a
347 follow-on paper, so the fit is not as clean as for Eris, and discrepancies are made more
348 conspicuous thanks to the very high signal to noise ratio (S/N) of the Makemake data. For
349 Makemake, we obtain best-fit parameters of D/H ratio 2.9×10^{-4}, methane grain sizes 1.2 and
350 0.06 cm (with the smaller particles representing 1.6% of the total, by volume), and $P_{(g)}$ equal to
351 1.8. The best fit model includes no N_2 or CO ice.
352 Uncertainties in the D/H ratios and other fitted parameters have various sources. Noise in
353 the spectra is not the main source of uncertainty for D/H, since the spectra have relatively high
354 signal-to-noise (S/N) where the CH_3D bands appear. The main source of uncertainty comes from
355 assumptions built into the radiative transfer model. It is necessary to choose a model
356 configuration with some number of free parameters, as well as a wavelength range to fit the
357 model to. Fitting to a larger wavelength range has the advantage of having more ordinary
358 methane bands of varying depths to better constrain the texture of the methane ice, and thus its
359 light scattering behavior that also applies to the CH_3D dispersed in the CH_4. But that assumes no
360 wavelength dependence of the scattering behavior such as occurs when there are textures at the
361 scale of the wavelength (e.g., Hapke 2012), and no effects of different scattering in different
362 regions of the surface, no vertical stratification, etc. To assess the uncertainty from model
363 assumptions, we tested a variety of model configurations. These included models with
364 wavelength- (λ) or w-dependent $P_{(g)}$, models using Hapke's internal scattering parameter s set to
365 a fitted constant multiplied by λ^{-4} representing Rayleigh scattering by defects within particles,
366 and models with three different particle sizes rather than two. Each model configuration was
367 fitted to various ranges of wavelengths. We found that for all these different combinations the
368 D/H ratio for each object varied within a band bounded by ±20%. The model presented in Fig. 2
369 is one that gave results near the middle of the range. We therefore report the D/H ratios for Eris
370 and Makemake as $(2.5 \pm 0.5) \times 10^{-4}$ and $(2.9 \pm 0.6) \times 10^{-4}$, respectively. For N_2 abundance on
371 Eris' surface, the range derived by the models was around 22 ± 5%, and for Makemake a few
372 models returned abundances as high as 3%, so this could be taken as a 1-σ upper limit.
373 We see no evidence for CO ice absorption in either spectrum, which is somewhat surprising
374 since it is readily seen in infrared spectra of Triton and Pluto (e.g., Cruikshank et al. 1993; Owen
375 et al. 1993). The fundamental vibrational absorption band in pure α CO occurs at 4.67 μm. With

376 the high S/N of the JWST spectra, and the absence of other spectral features at that wavelength, a
377 volumetric upper limit of about 2 parts per million of CO can be placed for Eris, and less than 1
378 part per million for Makemake. But we reiterate the caveat that the spectral behavior of CO
379 dissolved in CH_4 ice has not been studied in the laboratory. The vibrational band could be
380 broadened or shifted in wavelength in that molecular environment, potentially changing these
381 detection limits.
382 Small blue-shifts of a few Å in the CH_4 bands of Eris and Makemake have previously been
383 reported (e.g., Licandro et al. 2006a,b; Abernathy et al. 2009; Alvarez-Candal et al. 2011;
384 Lorenzi et al. 2015), and these shifts can be seen in the narrower methane bands in our JWST
385 data, too. When CH_4 molecules are dispersed in N_2 ice, their vibrational absorption bands appear
386 blue shifted (Quirico & Schmitt 1997b), but by a much larger amount than seen on Eris and
387 Makemake. By fitting for the relative abundances of a shifted and an un-shifted CH_4 component,
388 it is possible to estimate the fraction of CH_4 present in each phase. Where shifted and unshifted
389 components are both seen and thermodynamic equilibrium is assumed, the solubility limits from
390 the N_2-CH_4 binary phase diagram (Prokhvatilov & Yantsevich 1983) can be used to estimate the
391 abundance of N_2 ice required to account for the fraction of methane seen in each component.
392 Such an analysis was done for Eris (Tegler et al. 2010, 2012), implying a composition of 90% N_2
393 and 10% CH_4. That result is clearly at odds with the 22 ± 5% N_2 abundance we obtain from the
394 JWST observation of the N_2 fundamental vibrational band for Eris. Likewise, the few Å shifts
395 reported for Makemake's CH_4 bands attributed to the presence of N_2 could be seen as conflicting
396 with our 3% upper limit for N_2 in Makemake's JWST spectrum. Several factors may account for
397 these discrepancies, including the fact that small shifts in CH_4 bands have been found to occur
398 when small amounts of N_2 are dissolved into CH_4 without exceeding the solubility limit so that
399 no N_2 phase is present (Protopapa et al. 2015). Also, CH_4 bands can shift due to the presence of
400 other impurities, such as argon, that lacks its own characteristic absorption bands and may or
401 may not be present on Eris or Makemake (Tegler et al. 2010). Finally, as noted before, we lack
402 laboratory optical constants for the N_2 absorption band when it is dissolved in CH_4, though data
403 does exist for the CH_4 absorptions in such a mixture (Protopapa et al. 2015). Our ~22%
404 abundance is based on using optical constants of pure β N_2 ice. This number exceeds the ~4%
405 solubility limit (Prokhvatilov & Yantsevich 1983) of N_2 in CH_4 ice at Eris' ~30 K temperature,
406 implying that an N_2 phase should also be present on Eris, presumably the lower temperature α

phase. But relatively little CH_4 is soluble in α N_2 ice (approximately ~2%), so the presence of a small amount of this phase would have little effect on the appearance of the CH_4 bands. However, the shape of the N_2 fundamental band in α N_2 ice is somewhat different from that of β N_2, and is also temperature-dependent (Löwen et al. 1990; Schmitt et al. 1998). It can also be expected to be influenced by the presence of dissolved methane. More laboratory work is needed.

Replacing the carbon atom in methane with the heavier isotope ^{13}C does not change the symmetry of the molecule as occurs in CH_3D, but the additional mass does shift the vibrational absorptions to slightly longer wavelengths. Since most methane bands are broad compared to the scale of the shift, a small fraction of $^{13}CH_4$ relative to ordinary methane is not easy to detect. What is required is an especially narrow band with a rapid transition to much weaker absorption at slightly longer wavelengths where the $^{13}CH_4$ version of the band occurs. The 2.60 μm CH_4 band seen for the first time for Eris and Makemake in the JWST spectra has just these characteristics. From preliminary laboratory experiments, this band is red-shifted by 0.015 μm in $^{13}CH_4$ (W. Grundy personal communication). We shifted the ordinary CH_4 optical constants by this amount to simulate optical constants of $^{13}CH_4$ and performed similar models as described earlier for CH_3D to find the best fit $^{13}C/^{12}C$ ratios, using wavelengths between 2.57 and 2.65 μm. The best fit models are shown in Fig. 4, with $^{13}C/^{12}C$ ratios of 0.012 ± 0.002 and 0.010 ± 0.003 for Eris and Makemake, respectively. These numbers are not statistically distinguishable from each other nor from the terrestrial inorganic standard VPDB (Vienna Pee Dee Belemnite) $^{13}C/^{12}C$ ratio of 0.0112.

Finally, we should remark on the startlingly large particle sizes for methane ice in our models, 0.4 and 1.2 cm for Eris and Makemake, respectively. Such enormous particles are unusual in a planetary regolith, and might be more properly thought of as a measure of the optical mean free path between defects in a polycrystalline, sintered slab of ice, rather than granular particles. The paucity of N_2 and CO may aid production of such large optical path lengths by not interfering with sintering and grain growth of CH_4, especially on Makemake (e.g., Eluszkiewicz et al. 2007).

Geochemical interpretation and implications

We find D/H ratios in the methane ice of Eris and Makemake to be $(2.5 \pm 0.5) \times 10^{-4}$ and

$(2.9 \pm 0.6) \times 10^{-4}$, respectively. While there are unavoidable uncertainties in how observed values relate to starting or bulk values of D/H (e.g., Brown et al. 2012), our derived ratios can be compared with other reservoirs of hydrogen-bearing molecules in the solar system to gain some initial insight into what the data may be telling us about the origin of methane on Eris and Makemake (see Fig. 5). Eris and Makemake values are somewhat higher than the terrestrial VSMOW (Vienna Standard Mean Ocean Water) value (1.56×10^{-4}) and the D/H ratio of Titan's atmospheric methane (1.59×10^{-4}, Nixon et al. 2012), and are much higher than the bulk protoplanetary nebula value that was dominated by hydrogen gas (2.2×10^{-5}, e.g., Geiss & Gloeckler 2003; Aléon et al. 2022). But it is much lower than the 2.41×10^{-3} D/H ratio of methane measured in the coma of comet 67P/Churyomov-Gerasimenko (Müller et al. 2022) or 1.57×10^{-3} in the comet's refractory organic material (Paquette et al. 2021), not to mention isolated instances of extremely D-rich compositions in cometary and interplanetary dust particles (e.g., Aléon et al. 2001; McKeegan et al. 2006). Reduced carbon-bound hydrogen produced in the cold outer protosolar nebula or in interstellar environments generally appears to have high D/H ratios. This is a clue that methane seen on Eris and Makemake today was probably not delivered as a primordial species. These D/H differences point to different origins of methane. Eris' and Makemake's D/H ratios are similar to values determined for water and hydrated minerals in asteroids, comets, and larger icy bodies. This consistency suggests (but does not prove) that hydrogen atoms in the methane ice that is now frozen on the surfaces of Eris and Makemake originally came from a source of water. A subsurface ocean of liquid water is one possibility (Hussmann et al. 2006). Another possible source of water-like D/H ratios is phyllosilicate minerals. These could have formed during a period of water-rock differentiation (Nimmo & Brown 2023).

An important caveat to these comparisons is that the D/H ratios in different carrier molecules (water, methane, molecular hydrogen) are subject to potentially different fractionations during molecule formation and subsequent chemical processing. For example, Müller et al (2022) find that D/H in simple alkanes (including methane) are greater than in water in comet 67P. Therefore, the clues afforded by our broad comparison in Fig. 5 must be applied with caution. They can be placed on a firmer quantitative footing through modeling of D/H fractionation as described in the companion paper (Glein et al., submitted). Such modeling enables the D/H ratio of methane to provide a new window into the histories of Eris and

Makemake. A more penetrating perspective of these previously dimly understood bodies can be achieved by determining which geochemical sources of methane are consistent with our derived D/H ratios. We highlight the main D/H modeling results in this first paper for the sake of continuity and convenience. More detailed information can be found in Glein et al. (submitted). We also discuss here key geochemical implications of the broader composition, including the $^{13}C/^{12}C$ ratio.

Glein et al. (submitted) conducted a detailed investigation to assess whether Eris' and Makemake's surface methane inventories could be primordial, abiotic, or thermogenic. Primordial methane would have been acquired already in the form of methane (e.g., in accreted icy pebbles/planetesimals or via subsequent impact delivery). Abiotic methane (derived from CO_2 or CO) could be produced as a result of potential hydrothermal processes at the bottom of a subsurface ocean. We note that it is currently unclear how widespread abiotic methane is in water-rock systems on Earth (Etiope & Schoell 2014; Reeves & Fiebig 2020), although analogous systems in the outer solar system may be more conducive to abiotic synthesis if reduced nickel-bearing minerals are present to serve as catalysts (e.g., Glein 2015). Greater availability of CO (which is more reactive than CO_2) could also lead to more rapid CH_4 synthesis than typically encountered on Earth. Thermogenic methane would be produced by "cooking" accreted organic materials in a phyllosilicate-rich core that had undergone sufficient heating. If we can discriminate between these types of methane, then we can obtain useful information about formation conditions and processes that provide methane on icy dwarf planets.

Surprisingly, it was found that the simplest case of primordial methane is inconsistent with the data (Glein et al., submitted). If Eris' and Makemake's methane had a primordial origin, they would have high D/H ratios more like that of comet 67P (Müller et al. 2022). Instead, the observed D/H ratios point to a subsurface source that can generate abiotic or thermogenic methane. Since the production of both abiotic and thermogenic methane requires elevated temperatures to allow the necessary chemical reactions to occur, and because undifferentiated ice-rock mixtures at the relatively low pressures expected inside Eris (□15 kbar) and Makemake (□4 kbar) could not support such temperatures, we can conclude that their D/H ratios are evidence that these are differentiated planets with rocky cores that have been heated significantly (i.e., above a temperature of ~150°C; Stolper et al. 2014). Indeed, the synchronous spin state of Eris together with the low mass of its satellite further support Eris being a differentiated body

(Nimmo & Brown 2023). It should be noted that we cannot give more specific preference to abiotic or thermogenic methane on the basis of present data, as both types of methane can provide consistent D/H ratios.

Other volatiles observed or not detected by JWST also indicate the importance of evolutionary processes in shaping the present volatile inventories of Eris and Makemake. Our detection of N_2 on Eris is consistent with N_2 formation from a NH_3 or an organic N source in the interior (Glein 2023). In hypothesized seafloor hydrothermal fluids, N_2 production would be favored at higher temperatures and more oxidizing conditions, which could lead to CH_4 oxidation to CO_2 (Glein et al. 2008). We did not detect CO_2 on Eris, but there are conditions at which appreciable concentrations of N_2 and CH_4 can coexist at equilibrium (Glein et al. 2008). In addition, any CO_2 near the surface of Eris is likely covered by more volatile ices. Alternatively, Eris' N_2 could be associated with thermogenic processes in its inferred core. If conditions in the core were relatively hydrogen-poor, then the nitrogen speciation would be driven toward N_2 production (McKinnon et al. 2021).

On Makemake, JWST may not have detected N_2 owing to lower-temperature hydrothermal conditions (which would stabilize NH_3; Glein et al. 2008), as compared with Eris. Lower core temperatures would be consistent with the smaller size of Makemake. Another possibility is that Makemake might have previously had a CH_4-N_2 surface that evolved to a CH_4-rich surface by preferential escape of N_2. However, if Pluto is considered as an analogue, we might expect more CH_4 escape instead of N_2 escape (Young et al. 2018).

Hydrothermal geochemistry (e.g., Shock & McKinnon 1993) or early escape (e.g., Lunine & Nolan 1992) may explain a lack of CO on Eris and Makemake. Carbon monoxide is frequently the most abundant ice in comets after H_2O. Its extreme deficiency on Eris and Makemake would be hard to understand unless their present surface volatile compositions primarily reflect the role of evolution rather than primordial inheritance. The implication is that planet-sized Kuiper belt objects should not be regarded as "giant comets" that simply preserved their initial volatile inventories (cf. Glein & Waite 2018). Interior processes are called for to account for the D/H ratio in methane, and can also provide N_2 where it is present. Moreover, CO removal may be linked to CH_4 production if CO was a major carbon source of CH_4, as it is experimentally known to be (e.g., McCollom et al. 2010).

On the other hand, it may be more plausible to invoke early escape followed by volatile

replacement. In this case, it could be assumed that the lightest and most volatile primordial species (CH_4, N_2, and CO) were all lost. Thus, high-D/H methane would no longer be present. Early rather than later, more continuous escape is hypothesized to get rid of CO on Eris, as present surface conditions (even at perihelion) are not conducive to CO escape (Schaller & Brown 2007). After early escape, the interior would have heated up due to radiogenic heating (see Glein et al., submitted) until temperatures were sufficient to support endogenic production of CH_4 and N_2. These volatiles could have been trapped in clathrate hydrates that helped to keep the interior warm (e.g., Kamata et al., 2019), and eventually outgassed to the surface.

We determined carbon isotope ratios ($^{13}C/^{12}C$) of 0.012 ± 0.002 and 0.010 ± 0.003 for methane ice on Eris and Makemake, respectively. Carbon isotopes do not show much variability among solar system reservoirs. For example, methane in comet 67P/Churyumov-Gerasimenko has a $^{13}C/^{12}C$ ratio of 0.0114 ± 0.0013 (Müller et al. 2022), while the value for CO_2 is 0.0119 ± 0.0006 (Hässig et al. 2017). The protosolar value is thought to be ~0.0107 (Lyons et al. 2018), and organic matter in primitive carbonaceous chondrites has a $^{13}C/^{12}C$ ratio of ~0.0110 (Alexander et al. 2007). No matter how it originated, methane delivered to the surfaces of Eris and Makemake likely started with a $^{13}C/^{12}C$ ratio around 0.011. The fact that the present inventories of methane have ratios that are indistinguishable from this value implies that no large ^{13}C enrichment occurred on either body.

Over time, atmospheric escape (and photo/radiation chemistry to a lesser extent; Nixon et al. 2012) will increase the $^{13}C/^{12}C$ ratio because of preferential loss of $^{12}CH_4$ owing to its smaller mass (and weaker carbon-hydrogen bond). Perhaps the simplest way to keep the isotopic ratio "normal" is for escape (and photochemical fractionation) processes to operate over a short duration. If methane was delivered to the surface geologically recently, then there would not be enough time for the isotope ratio to evolve to heavy values. Continuous delivery of methane would work similarly in shifting the ratio toward a reset. These scenarios are appealing as they could also explain the high albedos of Eris and Makemake, which would otherwise darken due to photochemically driven synthesis of complex organics. A deep convecting "Sputnik planet" layer of methane ice might also be able to account for these observations, by mixing heavier radiolytic products down into a much larger methane reservoir and preventing them from accumulating at the surface. If the CH_4 ice reservoir is sufficiently large, the same might be true for a "bladed planet" scenario with seasonal volatile transport cycles maintaining an uppermost

561 visible surface dominated by lighter, more volatile species. With D/H ratios indicating an
562 endogenic origin of methane (Glein et al., submitted), it is plausible to envision geologically
563 recent outgassing processes delivering methane to the surface, analogous to previous proposals
564 for Pluto (Howard et al. 2023) and Titan (Tobie et al. 2006). From this perspective, Eris would
565 be more cryovolcanically active than Makemake, which would also be consistent with its less-
566 red coloration and lack of detectable ethane, whereas Makemake is redder and shows evidence of
567 irradiation products on its surface (Brown et al. 2007, 2015). On the other hand, the surface age
568 of Makemake's methane may not be substantially older than that of Eris' methane, as there is no
569 clear difference in their $^{13}C/^{12}C$ ratios.
570 Alternatively, Eris and Makemake may have relatively unevolved $^{13}C/^{12}C$ ratios because of
571 slow orbit-integrated loss rates of methane, or their surface inventories of methane may be large
572 so that loss processes have not made a noticeable dent in the isotopic ratio. Some combination of
573 these factors and "recent" outgassing may be at work instead. Ultimately, understanding what
574 recent, slow, and large mean for these worlds will require detailed evolutionary modeling to
575 define limiting values, similar to work that has been done on Titan (i.e., Mandt et al., 2012;
576 Nixon et al., 2012).

577 Summary and conclusion

578 Our JWST infrared spectrum of Eris shows, for the first time, clear evidence of absorption
579 by CH_3D in methane ice at 4.33 and 4.56 μm, a subtle feature at 2.615 μm due to $^{13}CH_4$, and
580 absorption by the fundamental band of N_2 ice between 4.0 and 4.3 μm. We also present the
581 spectrum of Makemake in the region of the above CH_3D and $^{13}CH_4$ bands. These data allow us
582 to estimate the D/H and $^{13}C/^{12}C$ ratios in methane on Eris and Makemake, and constrain the
583 abundance of N_2 ice on their surfaces. Unlike on Triton and Pluto, we find no evidence for CO
584 ice on Eris or Makemake, with upper limits in the parts per million range.
585 Similar isotopic results are expected in the near future for methane ice on Pluto and Triton,
586 and in water ice on Haumea and its family members, based on JWST spectra already in hand.
587 These studies are providing our first look at isotopic ratios for the planet-sized bodies beyond
588 Neptune with complex evolutionary histories and which appear to have undergone
589 differentiation. Thanks to JWST, our knowledge of these bodies is undergoing dramatic
590 advancement. More quantitative constraints on their histories will require future modeling of

subsurface geophysical/geochemical conditions and the fate of primordial volatiles, as well as detailed comparisons with Pluto and Triton. Much smaller comets and (active) Centaurs can provide comparable data for much less evolved bodies, albeit based primarily on isotopic ratios in the gas phase.

It is interesting that we can learn something useful about the internal structures and physical conditions in the deep interiors of such remote worlds by measuring isotopic ratios. This would not have been possible without the JWST data reported in this paper. It has also not escaped our attention that some subsurface circumstances suggested by our results (e.g., hydrothermal activity) could support the generation of chemical disequilibria (Amend et al. 2011; Waite et al. 2017). There may now be an observational basis to consider Eris in particular as a possible ocean world and as the most distant candidate for habitability in the solar system.

Acknowledgments

This work is based in part on observations made with the NASA/ESA/CSA James Webb Space Telescope. The data are at the MAST archive at STScI, which is operated by AURA, Inc., under NASA contract NAS 5-03127. These observations are associated with programs #1191 and #1254. We are especially grateful to Tony Roman, Shelly Meyett, and Charles Proffitt at STScI for help with program implementation. C.R.G. was supported by the NASA Astrobiology Institute through its JPL-led team entitled Habitability of Hydrocarbon Worlds: Titan and Beyond. J.A.S. acknowledges support through the sabbatical program at STScI, and the generosity of Lowell Observatory lodging in the Tombaugh apartment for 5 months, and NAU for office facilities during that time. H.B.H and S.N.M. acknowledge support from NASA JWST Interdisciplinary Scientist grant 21-SMDSS21-0013. R.B. acknowledges support from the CNES. N.P.A. acknowledges support from the Small Research Initiative of the Florida State operated by the Florida Space Institute. We also thank the free and open source software communities for empowering us with key tools used to complete this project, notably Linux, the GNU tools, LibreOffice, Evolution, Python, MariaDB, the Astronomy Users Library, and FVWM.

References

Abernathy, M.R., S.C. Tegler, W.M. Grundy, J. Licandro, W. Romanishin, D. Cornelison, and F.

620 Vilas 2009. Digging into the surface of the icy dwarf planet Eris. Icarus 199, 520-525.
621 Aléon, J., C. Engrand, F. Robert, and M. Chaussidon 2001. Clues to the origin of interplanetary
622 dust particles from the isotopic study of their hydrogen-bearing phases. Geochim.
623 Cosmochim. Acta 65, 4399-4412.
624 Aléon, J., D. Lévy, A. Aléon-Toppani, H. Bureau, H. Khodja, and F. Brisset 2022. Determination
625 of the initial hydrogen isotopic composition of the solar system. Nature Astron. 41550-
626 021-01595-7.1-6.
627 Alexander, C.M.O.D., M. Fogel, H. Yabuta, and G.D. Cody 2007. The origin and evolution of
628 chondrites recorded in the elemental and isotopic compositions of their macromolecular
629 organic matter. Geochim. Cosmochim. Acta 71, 4380-4403.
630 Alexander, C.M.O.D., R. Bowden, M.L. Fogel, K.T. Howard, C.D.K. Herd, and L.R. Nittler
631 2012. The provenances of asteroids, and their contributions to the volatile inventories of
632 the terrestrial planets. Science 337, 721-724.
633 Alvarez-Candal, A., N. Pinilla-Alonso, J. Licandro, J. Cook, E. Mason, T. Roush, D. Cruikshank,
634 F. Gourgeot, E. Dotto, and D. Perna 2011. The spectrum of (136199) Eris between 350
635 and 2350 nm: Results with X-Shooter. Astron. & Astrophys. 532, A130.
636 Amend, J.P., T.M. McCollom, M. Hentscher, and W. Bach 2011. Catabolic and anabolic energy
637 for chemolithoautotrophs in deep-sea hydrothermal systems hosted in different rock types.
638 Geochim. Cosmochim. Acta 75, 5736-5748.
639 Belskaya, I.N., S. Bagnulo, A. Stinson, G.P. Tozzi, K. Muinonen, Y.G. Shkuratov, M.A. Barucci,
640 and S. Fornasier 2012. Polarimetry of trans-neptunian objects (136472) Makemake and
641 (90482) Orcus. Astron. & Astrophys. 547, A101.
642 Bennett, C.J., C.S. Jamieson, Y. Osamura, and R.I. Kaiser 2006. Laboratory studies on the
643 irradiation of methane in interstellar, cometary, and solar system ices. Astrophys. J. 653,
644 792-811.
645 Bernstein, G.M., et al. (19 co-authors) 2023. Synchronous rotation in the (136199) Eris-
646 Dysnomia system. Planetary Sci. J. 4, 115.
647 Biver, N., et al. (16 co-authors) 2016. Isotopic ratios of H, C, N, O, and S in comets C/2012 F6
648 (Lemmon) and C/2014 Q2 (Lovejoy). Astron. & Astrophys. 589, A78.
649 Bockelée-Morvan, D., et al. (11 co-authors) 1998. Deuterated water in comet C/1996 B2
650 (Hyakutake) and its implications for the origin of comets. Icarus 133, 147-162.

651 Bockelée-Morvan, D., et al. (14 co-authors) 2015. Cometary isotopic measurements. Space Sci.
652 Rev. 197, 47-83.
653 Bohlin R.C., Gordon, K.D., and Tremblay, P.E. 2014. Techniques and review of absolute flux
654 calibration from the ultraviolet to the mid-infrared. Publ. Astron. Soc. Pacific, 126, 711-
655 732.
656 Brown, M.E. 2013. On the shape, size, and density of the dwarf planet Makemake. Astrophys.
657 J. Lett. 767, L7.
658 Brown, M.E., and E.L. Schaller 2007. The mass of dwarf planet Eris. Science 316, 1585-1585.
659 Brown, M.E., C.A. Trujillo, and D.L. Rabinowitz 2005. Discovery of a planetary-sized object in
660 the scattered Kuiper belt. Astrophys. J. 635, L97-L100.
661 Brown, M.E., K.M. Barkume, G.A. Blake, E.L. Schaller, D.L. Rabinowitz, H.G. Roe, and C.A.
662 Trujillo 2007. Methane and ethane on the bright Kuiper belt object 2005 FY_9. Astron. J.
663 133, 284-289.
664 Brown, M.E., E.L. Schaller, and G.A. Blake 2015. Irradiation products on dwarf planet
665 Makemake. Astron. J. 149, 105.
666 Brown, R.H., D.S. Lauretta, B. Schmidt, and J. Moores 2012. Experimental and theoretical
667 simulations of ice sublimation with implications for the chemical, isotopic, and physical
668 evolution of icy objects. Planet. Space Sci. 60, 166-180.
669 Brunetto, R., M.A. Barucci, E. Dotto, and G. Strazzulla 2006. Ion irradiation of frozen
670 methanol, methane, and benzene: Linking to the colors of Centaurs and trans-neptunian
671 objects. Astrophys. J. 644, 646-650.
672 Bushouse, H., et al. (25 co-authors) 2022. JWST calibration pipeline. Zenodo,
673 https://doi.org/10.5281/zenodo.6984366.
674 Calvani, P., S. Lupi, and P. Maselli 1989. The infrared spectrum of solid CD_4. J. Chem. Phys.
675 91, 6737-6742.
676 Calvani, P., S. Cunsolo, S. Lupi, and A. Nucara 1992. The near-infrared spectrum of solid CH_4.
677 J. Chem. Phys. 96, 7372-7379.
678 Carraro, G., M. Maris, D. Bertin, and M.G. Parisi 2006. Time series photometry of the dwarf
679 planet Eris (2003 UB_{313}). Astron. & Astrophys. 460, L39-L42.
680 Clark, R.N., R.H. Brown, D.P. Cruikshank, and G.A. Swayze 2019. Isotopic ratios of Saturn's
681 rings and satellites: Implications for the origin of water and Phoebe. Icarus 321, 791-802.

682 Cruikshank, D.P., T.L. Roush, T.C. Owen, T.R. Geballe, C. de Bergh, B. Schmitt, R.H. Brown,
683 and M.J. Bartholomew 1993. Ices on the surface of Triton. Science 261, 742-745.
684 Duffard, R., J.L. Ortiz, P. Santos Sanz, A. Mora, P.J. Gutiérrez, N. Morales, and D. Guirado
685 2008. A study of photometric variations on the dwarf planet (136199) Eris. Astron. &
686 Astrophys. 479, 877-881.
687 Dumas, C., F. Merlin, M.A. Barucci, C. de Bergh, O. Hainault, A. Guilbert, P. Vernazza, and A.
688 Doressoundiram 2007. Surface composition of the largest dwarf planet 136199 Eris (2003
689 UB_{313}). Astron. & Astrophys. 471, 331-334.
690 Ehrenfreund, P., A.C.A. Boogert, P.A. Gerakines, D.J. Jansen, W.A. Schutte, A.G.G.M. Tielens,
691 and E.F. van Dishoeck 1996. A laboratory database of solid CO and CO_2 for ISO. Astron.
692 & Astrophys. 315, L341-L344.
693 Eluszkiewicz, J., K. Cady-Pereira, M.E. Brown, and J.A. Stansberry 2007. Interpretation of the
694 near-IR spectra of the Kuiper belt object (136472) 2005 FY_9. J. Geophys. Res. 112,
695 E06003.
696 Etiope, G., and M. Schoell 2014. Abiotic gas: Atypical, but not rare. Elements 10, 291-296.
697 Ewing, G.E. 1964. Infrared absorption of the ν_3 fundamental of liquid and solid CH_4 and CD_4.
698 J. Chem. Phys. 40, 179-183.
699 Geiss, J., and G. Gloeckler 2003. Isotopic compostion of H, He, and Ne in the protosolar cloud.
700 Space Sci. Rev. 106, 3-18.
701 Gerakines, P.A., and R.L. Hudson 2020. A modified algorithm and open-source computational
702 package for the determination of infrared optical constants relevant to astrophysics.
703 Astrophys. J. 901, 52.
704 Glein, C.R. 2015. Noble gases, nitrogen, and methane from the deep interior to the atmosphere
705 of Titan. Icarus 250, 570-586.
706 Glein, C.R. 2023. N_2 accretion, metamorphism of organic nitrogen, or both processes likely
707 contributed to the origin of Pluto's N_2. Icarus 404, 115651.
708 Glein, C.R., and J.H. Waite 2018. Primordial N_2 provides a cosmochemical explanation for the
709 existence of Sputnik Planitia, Pluto. Icarus 313, 79-92.
710 Glein, C.R., M.Y. Zolotov, and E.L. Shock 2008. The oxidation state of hydrothermal systems
711 on early Enceladus. Icarus 197, 157-163.
712 Glein, C.R., W.M. Grundy, J.I. Lunine, I. Wong, S. Protopapa, N. Pinilla-Alonso, J.A. Stansberry,

B.J. Holler, J.C. Cook, and A.C. Souza-Feliciano. Moderate D/H ratios in methane ice on Eris and Makemake as evidence of hydrothermal or metamorphic processes in their interiors: Geochemical analysis. Icarus (submitted).

Grundy, W.M. 2019. Pluto and Charon as templates for other large transneptunian objects. In: D. Prialnik, M.A. Barucci, L.A. Young (Eds.), *The Trans-Neptunian Solar System*, Elsevier, Cambridge MA, 291-305.

Grundy, W.M., B. Schmitt, and E. Quirico 2002. The temperature-dependent spectrum of methane ice I between 0.7 and 5 μm and opportunities for near-infrared remote thermometry. Icarus 155, 486-496.

Grundy, W.M., S.J. Morrison, M.J. Bovyn, S.C. Tegler, and D.M. Cornelison 2011. Remote sensing D/H ratios in methane ice: Temperature-dependent absorption coefficients of CH_3D in methane ice and in nitrogen ice. Icarus 212, 941-949.

Grundy, W.M., and O.M. Umurhan 2017. Are Eris and Makemake Sputnik planets? DPS #49, abstract 202.02.

Grundy, W.M., et al. (39 co-authors) 2018. Pluto's haze as a surface material. Icarus 314, 232-245.

Hapke, B. 2012. *Theory of reflectance and emittance spectroscopy.* 2nd edition, Cambridge University Press, New York.

Hartogh, P., et al. (12 co-authors) 2011. Ocean-like water in the Jupiter-family comet 103P/Hartley 2. Nature 478, 218-220.

Hässig, M., et al. (17 co-authors) 2017. Isotopic composition of CO_2 in the coma of 67P/Churyumov-Gerasimenko measured with ROSINA/DFMS. Astron. & Astrophys. 605, A50.

Heinze, A.N., and D. deLahunta 2009. The rotation period and light-curve amplitude of Kuiper belt dwarf planet 136472 Makemake (2005 FY_9). Astron. J. 138, 428-438.

Hofgartner, J.D., B.J. Buratti, P.O. Hayne, and L.A. Young 2019. Ongoing resurfacing of KBO Eris by volatile transport in local, collisional, sublimation atmosphere regime. Icarus 334, 52-61.

Hofgartner, J.D., et al. (11 co-authors) 2023. Bolometric hemispherical albedo map of Pluto from New Horizons observations. Planetary Sci. J. 4, 132.

Holler, B.J., W.M. Grundy, M.W. Buie, and K.S. Noll 2021. The Eris/Dysnomia system I: The

orbit of Dysnomia. Icarus 355, 114130.

Howard, A.D., J.M. Moore, O.M. Umurhan, O.L. White, K.N. Singer, and P.M. Schenk 2023. Are the surface textures of Pluto's Wright Mons and its surroundings exogenic? Icarus 405, 115719.

Hromakina, T.A., et al. (19 co-authors) 2019. Long-term photometric monitoring of the dwarf planet (136472) Makemake. Astron. & Astrophys. 625, A46.

Hussmann, H., F. Sohl, and T. Spohn 2006. Subsurface oceans and deep interiors of medium-sized outer planet satellites and large trans-neptunian objects. Icarus 185, 258-273.

Johnson, R.E., A. Oza, L.A. Young, A.N. Volkov, and C. Schmidt 2015. Volatile loss and classification of Kuiper belt objects. Astrophys. J. 809, 43.

Kamata, S., F. Nimmo, Y. Sekine, K. Kuramoto, N. Noguchi, J. Kimura, and A. Tani 2019. Pluto's ocean is capped and insulated by gas hydrates. Nature Geosci. 12, 407-410.

Licandro, J., N. Pinilla-Alonso, M. Pedani, E. Oliva, G.P. Tozzi, and W.M. Grundy 2006a. The methane ice rich surface of large TNO 2005 FY_9: a Pluto-twin in the trans-neptunian belt? Astron. & Astrophys. 445, L35-L38.

Licandro, J., W.M. Grundy, N. Pinilla-Alonso, and P. Leisy 2006b. Visible spectroscopy of 2003 UB_{313}: Evidence for N_2 ice on the surface of the largest TNO? Astron. & Astrophys. 458, L5-L8.

Lis, D.C., D. Bockelée-Morvan, R. Güsten, N. Biver, J. Stutzki, Y. Delorme, C. Durán, H. Wiesemeyer, and Y. Okado 2019. Terrestrial deuterium-to-hydrogen ratio in water in hyperactive comets. Astron. & Astrophys. 625, L5.

Lorenzi, V., N. Pinilla-Alonso, and J. Licandro 2015. Rotationally resolved spectroscopy of dwarf planet (136472) Makemake. Astron. & Astrophys. 577, A86.

Löwen, H.W., K.D. Bier, and H.J. Jodl 1990. Vibron-phonon excitations in the molecular crystals N_2, O_2, and CO by Fourier transform infrared and Raman studies. J. Chem. Phys. 93, 8565-8575.

Lunine, J.I., and M.C. Nolan 1992. A massive early atmosphere on Triton. Icarus 100, 221-234.

Lyons, J.R., E. Gharib-Nezhad, and T.R. Ayres 2018. A light carbon isotope composition for the Sun. Nature Commun. 9, 908.

Mandt, K.E., J.H. Waite Jr., B. Teolis, B.A. Magee, J. Bell, J.H. Westlake, C.A. Nixon, O. Mousis, and J.I. Lunine 2012. The $^{12}C/^{13}C$ ratio on Titan from Cassini INMS

measurements and implications for the evolution of methane. Astrophys. J. 749, 160.

Maris, M., and G. Carraro 2008. An analysis of the Eris (2003 UB_{313}) light curve. Planet. Space Sci. 56, 1874-1877.

McCollom, T.M., B.S. Lollar, G. Lacrampe-Couloume, and J.S. Seewald 2010. The influence of carbon source on abiotic organic synthesis and carbon isotope fractionation under hydrothermal conditions. Geochim. Cosmochim. Acta 74, 2717-2740.

McKeegan, K.D., et al. (46 co-authors) 2006. Isotopic compositions of cometary matter returned by Stardust. Science 314, 1724-1728.

McKinnon, W.B., et al. (14 co-authors) 2016. Convection in a volatile nitrogen-ice-rich layer drives Pluto's geological vigour. Nature 534, 82-85.

McKinnon, W.B., C.R. Glein, T. Bertrand, and A.R. Rhoden 2021. Formation, composition, and history of the Pluto system: a post-New-Horizons synthesis. In: Stern, S.A., et al. (Eds.), *The Pluto System after New Horizons*. Univ. of Arizona Press, Tucson, AZ, pp. 507-543.

Meier, R., T.C. Owen, D.C. Jewitt, H.E. Matthews, M. Senay, N. Biver, D. Bockelée-Morvan, J. Crovisier, and D. Gautier 1998a. Deuterium in comet C/1995 O1 (Hale-Bopp): Detection of DCN. Science 279, 1707-1710.

Meier, R., T.C. Owen, H.E. Matthews, D.C. Jewitt, D. Bockelée-Morvan, N. Biver, J. Crovisier, and D. Gautier 1998b. A determination of the HDO/H_2O ratio in comet C/1995 O1 (Hale-Bopp). Science 279, 842-844.

Merlin, F., A. Alvarez-Candal, A. Delsanti, S. Fornasier, M.A. Barucci, F.E. DeMeo, C. de Bergh, A. Doressoundiram, E. Quirico, and B. Schmitt 2009. Stratification of methane ice on Eris' surface. Astron. J. 137, 315-328.

Moore, J.M., et al. (15 co-authors) 2017. Sublimation as a landform-shaping process on Pluto. Icarus 287, 320-333.

Moseley, S., R.G. Arendt, D. Fixsen, D. Lindler, M. Loose, and B.J. Rauscher 2010. Reducing the read noise of H2RG detector arrays: eliminating correlated noise with efficient use of reference signals. SPIE, 7742, 77421B.

Mueller, T., E. Lellouch, and S. Fornasier 2019. Trans-neptunian objects and Centaurs at thermal wavelengths. In: D. Prialnik, M.A. Barucci, L.A. Young (Eds.), *The Trans-Neptunian Solar System*, Elsevier, Cambridge MA, 153-181.

Müller, D.R., K. Altwegg, J.J. Berthelier, M. Combi, J. De Keyser, S.A. Fuselier, N. Hänni, B.

Prestoni, M. Rubin, I.R.H.G. Schroeder I, and S.F. Wampfler 2022. High D/H ratios in water and alkanes in comet 67P/Churyumov-Gerasimenko measured with Rosetta/ROSINA DFMS. Astron. & Astrophys. 662, A69.

Nelder, J., and R. Mead 1965. A simplex method for function minimization. Computer Journal 7, 308-313.

Nimmo, F., et al. (16 co-authors) 2017. Mean radius and shape of Pluto and Charon from New Horizons images. Icarus 287, 12-29.

Nimmo, F. and M.E. Brown 2023. The internal structure of Eris inferred from its spin and orbit evolution. Science Adv. 9, eadi9201.

Nixon, C.A., et al. (12 co-authors) 2012. Isotopic ratios in Titan's methane: Measurements and modeling. Astrophys. J. 749, 159.

Olkin, C.B., C.J.A. Howett, S. Protopapa, W.M. Grundy, A.J. Verbiscer, and M.W. Buie 2021. Colors and photometric properties of Pluto. In: S.A. Stern, J.M. Moore, W.M. Grundy, L.A. Young, R.P. Binzel (Eds.), *The Pluto System After New Horizons*, University of Arizona Press, Tucson, 147-163.

Ortiz, J.L., P. Santos Sanz, P.J. Gutiérrez, R. Duffard, and F.J. Aceituno 2007. Short-term rotational variability in the large TNO 2005FY$_9$. Astron. & Astrophys. 468, L13-L16.

Ortiz, J.L., et al. (55 co-authors) 2012. Albedo and atmospheric constraints of dwarf planet Makemake from a stellar occultation. Nature 491, 566-569.

Owen, T.C., T.L. Roush, D.P. Cruikshank, J.L. Elliot, L.A. Young, C. de Bergh, B. Schmitt, T.R. Geballe, R.H. Brown, and M.J. Bartholomew 1993. Surface ices and atmospheric composition of Pluto. Science 261, 745-748.

Paganini, L., M.J. Mumma, E.L. Gibb, and G.L. Villanueva 2017. Ground-based detection of deuterated water in comet C/2014 Q2 (Lovejoy) at IR wavelengths. Astrophys. J. Lett. 836, L25.

Paquette, J.A., et al. (13 co-authors) 2021. D/H in the refractory organics of comet 67P/Churyumov-Gerasimenko measured by Rosetta/COSIMA. Mon. Not. R. Astron. Soc. 504, 4940-4951.

Parker, A.H., M.W. Buie, W.M. Grundy, and K.S. Noll 2016. Discovery of a Makemakean moon. Astrophys. J. Lett. 825, L9.

Piani, L., Y. Marrocchi, L.G. Vacher, H. Yurimoto, and M. Bizzarro 2012. Origin of hydrogen

837 isotopic variations in chondritic water and organics. Earth & Planet. Sci. Lett. 567,
838 117008.
839 Piani, L., H. Yurimoto, and L. Remusat 2018. A dual origin for water in carbonaceous asteroids
840 revealed by CM chondrites. Nature Astron. 2, 317-323.
841 Piani, L., et al. (87 co-authors) 2023. Hydrogen isotopic composition of hydrous minerals in
842 asteroid Ryugu. Astrophys. J. Lett. 946, L43.
843 Prokhvatilov, A.I., and L.D. Yantsevich 1983. X-ray investigation of the equilibrium phase
844 diagram of CH_4-N_2 solid mixtures. Sov. J. Low Temp. Phys. 9, 94-98.
845 Protopapa, S., W.M. Grundy, S.C. Tegler, and J.M. Bergonio 2015. Absorption coefficients of
846 the methane-nitrogen binary ice system: Implications for Pluto. Icarus 253, 179-188.
847 Protopapa, S., et al. (19 co-authors) 2020. Disk-resolved photometric properties of Pluto and the
848 coloring materials across its surface. Astron. J. 159, 74.
849 Quirico, E., and B. Schmitt 1997a. A spectroscopic study of CO diluted in N_2 ice: Applications
850 for Triton and Pluto. Icarus 128, 181-188.
851 Quirico, E., and B. Schmitt 1997b. Near-infrared spectroscopy of simple hydrocarbons and
852 carbon oxides diluted in solid N_2 and as pure ices: Implications for Triton and Pluto.
853 Icarus 127, 354-378.
854 Rauscher, B.J., R.G. Arendt, D.J. Fixsen, M. Lander, D. Lindler, M. Loose, S.H. Moseley, D.V.
855 Wilson, and C. Xenophontos 2012. Reducing the read noise of HAWAII-2RG detector
856 systems with improved reference sampling and subtraction (IRS^2). SPIE, 8453, 84531F.
857 Reeves, E.P., and J. Fiebig 2020. Abiotic synthesis of methane and organic compounds in
858 Earth's lithosphere. Elements 16, 25-31.
859 Roe, H.G., R.E. Pike, and M.E. Brown 2008. Tentative detection of the rotation of Eris. Icarus
860 198, 459-464.
861 Schaller, E.L., and M.E. Brown 2007. Volatile loss and retention on Kuiper belt objects.
862 Astrophys. J. 659, L61-L64.
863 Schmitt, B., C. de Bergh, E. Lellouch, J.P. Maillard, A. Barbe, and S. Douté 1994. Identification
864 of three absorption bands in the two micron spectrum of Io. Icarus 111, 79-105.
865 Schmitt, B., E. Quirico, F. Trotta, and W.M. Grundy 1998. Optical properties of ices from UV to
866 infrared. In: B. Schmitt, C. de Bergh, M. Festou (Eds.), *Solar System Ices*, Kluwer
867 Academic Publishers, Boston, 199-240.

868 Schriver-Mazzuoli, L., H. Chaabouni, and A. Schriver 2003. Infrared spectra of SO_2 and
869 SO_2:H_2O ices at low temperature. J. Molecular Structure 644, 151-164.
870 Shapiro, M.M., and H.P. Gush 1966. The collision-induced fundamental and first overtone bands
871 of oxygen and nitrogen. Can. J. Phys. 44, 949-963.
872 Shock, E.L., and W.B. McKinnon 1993. Hydrothermal processing of cometary volatiles –
873 applications to Triton. Icarus 106, 464-477.
874 Sicardy, B., et al. (72 co-authors) 2011. A Pluto-like radius and a high albedo for the dwarf
875 planet Eris from an occultation. Nature 478, 493-496.
876 Stern, S.A., L.M. Trafton, and G.R. Gladstone 1988. Why is Pluto bright? Implications of the
877 albedo and lightcurve behavior of Pluto. Icarus 75, 485-498.
878 Stern, S.A., W.M. Grundy, W.B. McKinnon, H.A. Weaver, and L.A. Young 2018. The Pluto
879 system after New Horizons. Ann. Rev. Astron. & Astrophys. 56, 357-391.
880 Stolper, D.A., et al. (11 co-authors) 2014. Formation temperatures of thermogenic and biogenic
881 methane. Science 344, 1500-1503.
882 Szakáts, R., et al. (11 co-authors) 2023. Tidally locked rotation of the dwarf planet (136199) Eris
883 discovered via long-term ground-based and space photometry. Astron. & Astrophys. 669,
884 L3.
885 Tegler, S.C., W.M. Grundy, W. Romanishin, G.J. Consolmagno, K. Mogren, and F. Vilas 2007.
886 Optical spectroscopy of the large Kuiper belt objects 136472 (2005 FY_9) and 136108
887 (2003 EL_{61}). Astron. J. 133, 526-530.
888 Tegler, S.C., W.M. Grundy, F. Vilas, W. Romanishin, D. Cornelison, and G.J. Consolmagno, S.J.
889 2008. Evidence of N_2-ice on the surface of the icy dwarf planet 136472 (2005 FY_9).
890 Icarus 195, 844-850.
891 Tegler, S.C., D.M. Cornelison, W.M. Grundy, W. Romanishin, M.R. Abernathy, M.J. Bovyn, J.A.
892 Burt, D.E. Evans, C.K. Maleszewski, Z. Thompson, and F. Vilas 2010. Methane and
893 nitrogen abundances on Pluto and Eris. Astrophys. J. 725, 1296-1305.
894 Tegler, S.C., W.M. Grundy, C.B. Olkin, L.A. Young, W. Romanishin, D.M. Cornelison, and R.
895 Khodadadkouchaki 2012. Ice mineralogy across and into the surfaces of Pluto, Triton, and
896 Eris. Astrophys. J. 751, 76.
897 Thompson, W.R., B.G.J.P.T. Murray, B.N. Khare, and C. Sagan 1987. Coloration and darkening
898 of methane clathrate and other ices by charged particle irradiation: Applications to the

outer solar system. J. Geophys. Res. 92, 14933-14947.

Tobie, G., J.I. Lunine, and C. Sotin 2006. Episodic outgassing as the origin of atmospheric methane on Titan. Nature 440, 61-64.

Trafton, L.M., D.L. Matson, and J.A. Stansberry 1998. Surface/atmosphere interactions and volatile transport (Triton, Pluto, and Io). In: B. Schmitt, C. de Bergh, M. Festou (Eds.), *Solar System Ices*, Kluwer Academic, Dordrecht, 773-812.

Van Kranendonk, J. 1957. Theory of induced infra-red absorption. Physica 23, 825-837.

Villanueva, G.L., M.D. Smith, S. Protopapa, S. Faggi, and A.M. Mandell 2018. Planetary Spectrum Generator: An accurate online radiative transfer suite for atmospheres, comets, small bodies and exoplanets. J. Quant. Spectrosc. Radiat. Transf. 217, 86-104.

Villanueva, G.L., G. Luizzi, S. Faggi, S. Protopapa, V. Kofman, T. Fauchez, S.W. Stone, and A.M. Mandell 2022. *Fundamentals of the Planetary Spectrum Generator*. NASA Goddard Space Flight Center, ISBN 978-0-578-36143-7.

Verbiscer, A.J., et al. (17 co-authors) 2022. The diverse shapes of dwarf planet and large KBO phase curves observed from New Horizons. Planetary Sci. J. 3, 95.

Waite Jr., J.H., et al. (15 co-authors) 2009. Liquid water on Enceladus from observations of ammonia and ^{40}Ar in the plume. Nature 460, 487-490.

Waite, J.H., et al. (12 co-authors) 2017. Cassini finds molecular hydrogen in the Enceladus plume: evidence for hydrothermal processes. Science 356, 155-159.

Young, L.A., et al. (25 co-authors) 2018. Structure and composition of Pluto's atmosphere from the New Horizons solar ultraviolet occultation. Icarus 300, 174-199.

Figures

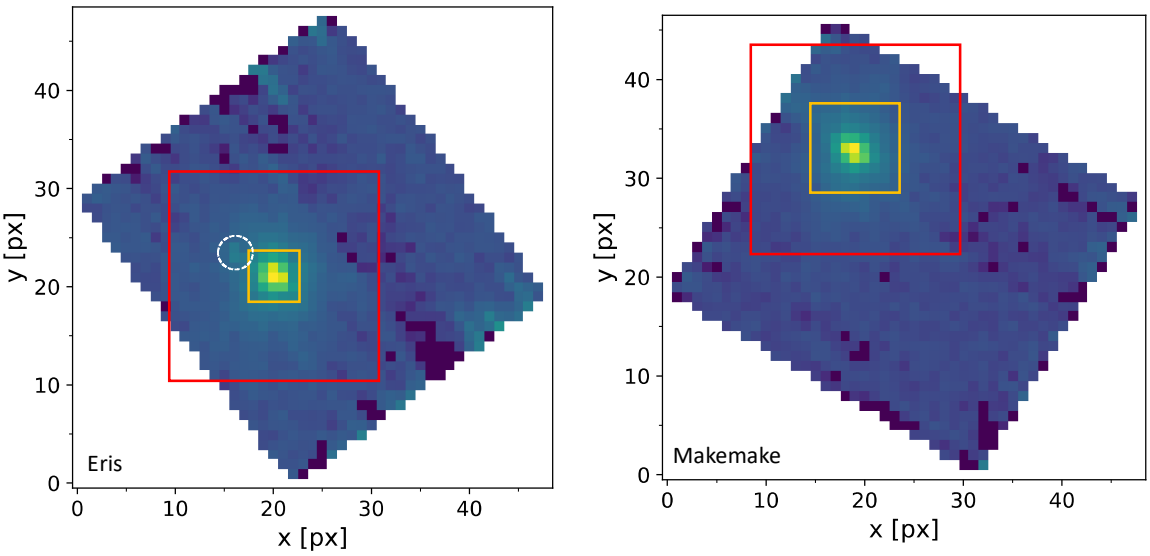

Figure 1: Wavelength-collapsed NIRSpec IFU cubes of Eris and Makemake from one of the two G140M observations. The outer and inner boundaries of the flux extraction and background regions used to produce the spectra presented in this paper are denoted by the yellow and red boxes with sides of length L_a and L_b, respectively, 5 and 20 pixels for Eris and 9 and 20 pixels for Makemake. Eris' small satellite Dysnomia is marked by the dashed white circle. Makemake's satellite is too faint to be seen here, and too faint to contribute meaningfully to the spectrum.

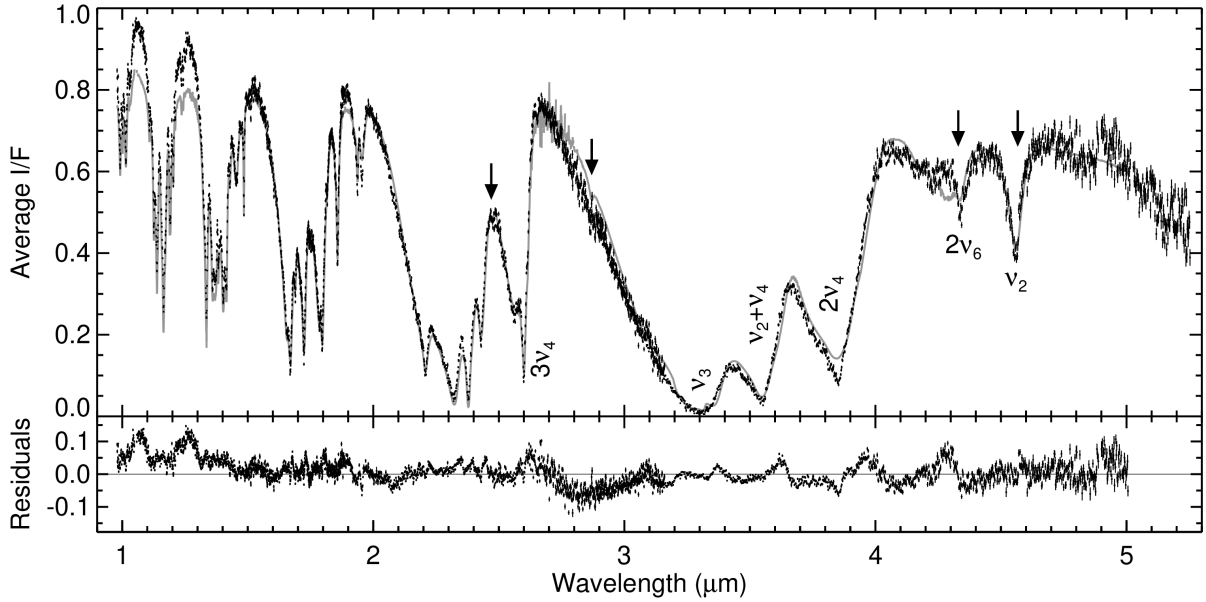

927 **Figure 2:** JWST Eris spectrum (black points) and model (gray curve). Methane absorption
928 bands not previously measured for Eris are labeled, with locations of deuterated methane bands
929 indicated by arrows. The model was fitted to data between 1.4 and 4.8 μm, so the residuals
930 (bottom panel) are larger outside of that range. The model was only calculated out to 5 μm,
931 owing to limits in available optical constants. Noise in the model spectrum between 2.63 and
932 2.83 μm is due to contamination of the CH_4 ice laboratory data by water vapor absorption lines.

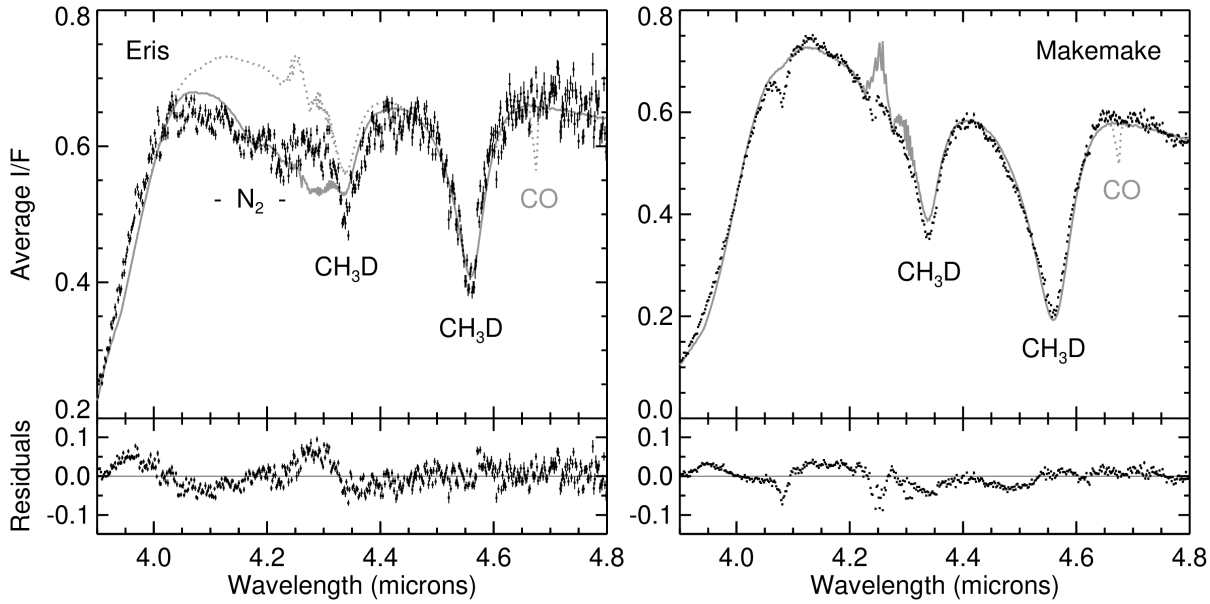

933 **Figure 3:** Spectra and models for Eris (left panel) and Makemake (right panel) zoomed in
934 on the region of the strong CH_3D bands. Dotted curves showing narrow features at 4.67 μm
935 have trace amounts of CO ice added in the model: 2 parts per million by volume for Eris and
936 1 ppm for Makemake, quantities that would have been detected if they had been present. The
937 dotted curve in the Eris panel with higher reflectance values between 4.0 and 4.3 μm shows the
938 effect of removing the N_2 ice. Apparent features in the model spectra between 4.23 and 4.33 μm
939 should be ignored. They are due to poor removal of gas phase CO_2 absorption from the
940 laboratory absorption data for CH_4 ice. The band at 4.08 μm in the Makemake spectrum is a
941 component that is absent from our models, possibly SO_2 (e.g., Schmitt et al. 1994, 1998;
942 Schriver-Mazzuoli et al. 2003).

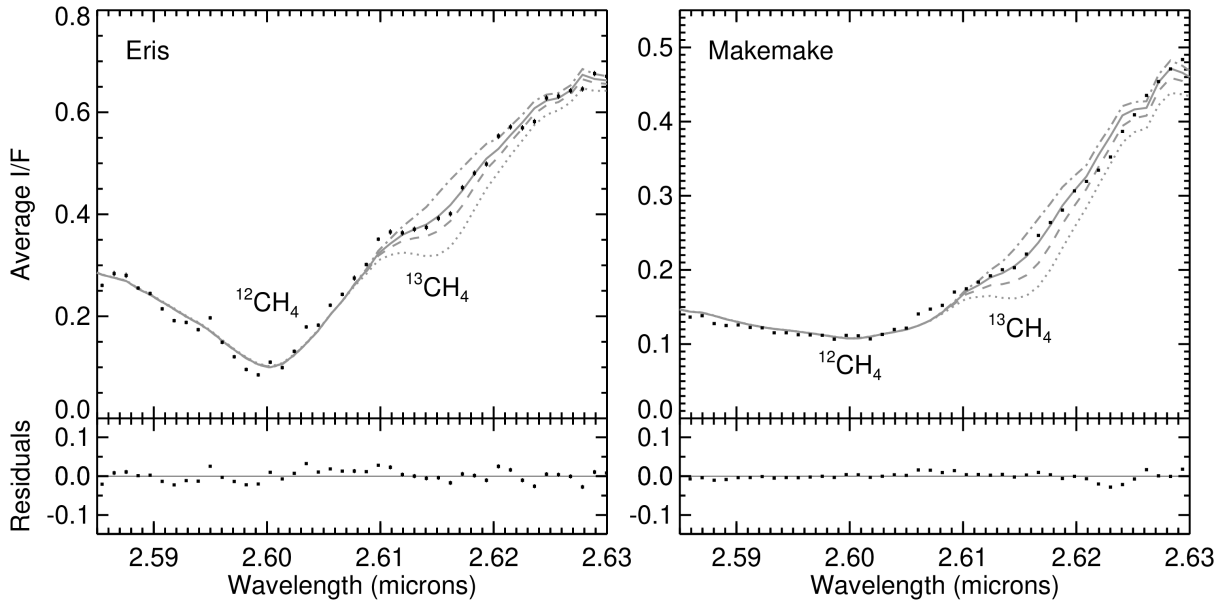

Figure 4: Close-up view of the $3\nu_4$ $^{12}CH_4$ band at 2.60 µm and its $^{13}CH_4$ counterpart at 2.615 µm. The Eris (left panel) and Makemake (right panel) data are shown as points with error bars. Best fit models are shown with solid curves with $^{13}C/^{12}C$ ratios of 0.012 and 0.010 for Eris and Makemake, respectively. Models with no $^{13}CH_4$ are shown with dot-dashed curves, models with twice the 0.0112 solar system average are shown as dashed curves, and models with four times are shown as dotted curves. Our JWST data are consistent with previously reported blue shifts in the methane bands of a few Å, though such a small shift is difficult to discern in this plot where the small ticks on the wavelength axes are at 10 Å intervals.

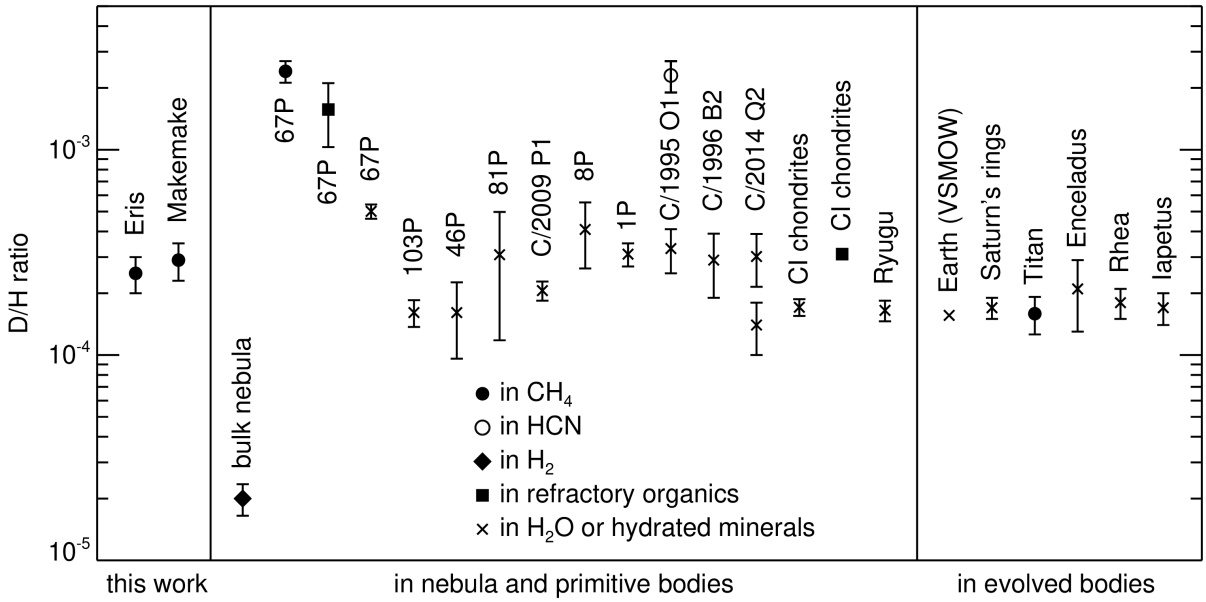

951 **Figure 5:** Eris and Makemake D/H ratios are greatly enriched compared with the bulk
952 protoplanetary nebula (Geiss & Gloeckler 2003; Aléon et al. 2022), but much less enriched than
953 methane, HCN, or refractory organics in comets C/1995 O1 Hale-Bopp or 67P/Churyumov-
954 Gerasimenko (Meier et al. 1998a; Bockelée-Morvan et al. 2015; Paquette et al. 2021; Müller et
955 al. 2022). They are more consistent with D/H ratios in water in comets (Bockelée-Morvan et al.
956 1998, 2015; Meier et al. 1998b; Hartogh et al. 2011; Biver et al. 2016; Paganini et al. 2017; Lis
957 et al. 2019). Hydrated minerals in CI chondrite meteorites and Ryugu (Piani et al. 2012, 2018,
958 2023) are a little lower, similar to ratios in H_2O in Earth and the Saturn system (Waite Jr. et al.
959 2009; Clark et al. 2019), plus CH_4 in Titan's atmosphere (Nixon et al. 2012), while refractory
960 organics in CI chondrites are more enriched (Alexander et al. 2007, 2012).